Talanta 221 (2021) 121560

Contents lists available at ScienceDirect

Talanta

journal homepage: www.elsevier.com/locate/talanta

New Bi_2MoO_6 nano-shapes toward ultrasensitive enzymeless glucose tracing: Synergetic effect of the Bi-Mo association

Avideh Khazraei [a], Aliakbar Tarlani [a,*], Mahboube Eslami-Moghadam [a], Jacques Muzart [b]

[a] Chemistry & Chemical Engineering Research Center of Iran, Pajoohesh Blvd., Km 17, Karaj Hwy, Tehran, 14968-13151, Iran
[b] Institut de Chimie Moléculaire de Reims, CNRS-Université de Reims Champagne-Ardenne, BP 1039, 51687, Reims Cedex 2, France

ARTICLE INFO

Keywords:
γ-Bi_2MoO_6
Mixed metal oxides
Semiconductor
Glucose
Non-enzymatic

ABSTRACT

In a novel approach, an efficient non-enzymatic glucose sensor based on pure phase of aurivillius bismuth molybdate (BM or γ-Bi_2MoO_6) mixed metal oxides is reported. Three BM samples were synthesized, with/without L-cysteine (Cys) and dodecylamine (DDA) as additives, leading to different shapes: bullet (BM-C), confetti (BM-2Cys) and candy (BM-2DDA). The morphology and purity of the structures were confirmed by FE-SEM images and XRD. In order to investigate the sensor application, the samples were integrated on reduced graphene oxide and incorporated into simple and inexpensive glassy carbon electrode (GCE) without using any polyvinylpyrrolidone (PVP) or Nafion. To perform cyclic voltammetry experiments, all three biosensors were measured in PBS solution (pH = 7) in ±1.5 voltage range and 50 mV s^{-1} scan rate. Glucose identification by the synthesized composites is an obvious sign of their high efficiency. According to chronoamperomograms, the best sensitivity of 3050 μA L $mmol^{-1}$ cm^{-2} with linear range of 0.02–0.14 mmol L^{-1}, low detection limit (LOD) of 0.004 mmol L^{-1} and the signal/noise equal to 3 was achieved by BM-2DDA/rGO/GCE biosensor and its speedy amperometric response is less than 5 s. This biosensor showed impressive selectivity, repeatability and reproducibility results besides it maintains its stability considerably in great percentage of 98.5% after eight weeks. Also it showed prolonged stability after 50 min.

1. Introduction

Diabetes is a metabolic disease which causes an abnormal blood sugar level [1], which subsequently activates some metabolic pathways resulting inflammation and apoptosis [2]. Its complications are coronary artery stenosis, peripheral vascular disease, stroke, kidney failure and blindness [3]. More than 385 million people worldwide are suffering from diabetes and this number increases yearly [4]. According to international diabetes federation (IDF) report, it is estimated that in 2019, around 4.2 million people from age 20 to 79 died from diabetes that means one death every 7 s [5]. Therefore, diabetes diagnosis and blood sugar control are vital to reduce death rate [6].

There are several methods of glucose detection such as colorimetry, electrochemical, optical and fluorescent. Besides being portable and low-cost, electrochemical sensors possess the advantages of high sensitivity and selectivity over other methods and have been used for almost last decade to detect glucose in blood [7,8]. Furthermore, electrochemical technique has high detection limit, reliability and rapid response [9,10]. In recent years, enzymatic electrochemical glucose sensors were one of the suitable detective devices. But because of some disadvantages like high manufacturing cost, lack of thermal stability (upper than 40 °C), pH sensitivity (losing activity in pH<2 and pH>8) and sensitivity to chemical substances within solution, enzymatic electrochemical sensors have been replaced by non-enzymatic ones [11–13]. In these sensors, the oxidation of glucose on the electrode surface [14] not only necessitate glucoses and electrons transportation, but also a fast and efficient redox reaction on the surface of electrode/electrolyte [15]. Furthermore, a key factor for non-enzymatic high performance electrochemical sensors is choosing appropriate active electrocatalyst. For this reason, use of metal oxide nanostructures with high surface area, high catalytic performance, effective electron transportation, low cost and good biocompatiblity such as ZnO [16], CuO [17,18], $NiWO_4$ [19], $CuCo_2O_4$ [20], $NiCo_2O_4$ [21] is an effective strategy.

Bismuth molybdate (Bi_2O_3.$nMoO_3$, n = 1, 2 and 3) can be classified into –γBi_2MoO_6, β-$Bi_2Mo_2O_9$ and α-$Bi_2Mo_3O_{12}$ phases [22,23]. n-Type semiconductor γ-Bi_2MoO_6 has aurivillius structure in which Bi is surrounded with octahedral MoO_6 grid and forms $(Bi_2O_2)^{+2}$ layers parallelly in perovskite MoO_4^{-2}, that results in little band gap (2.5–2.8 eV)

* Corresponding author.
E-mail address: Tarlani@ccerci.ac.ir (A. Tarlani).

https://doi.org/10.1016/j.talanta.2020.121560
Received 29 June 2020; Received in revised form 9 August 2020; Accepted 10 August 2020
Available online 3 September 2020

[24,25]. In gamma phase, molybdenum has flawless octahedral coordination which leads to creation of different catalytic active sites [26]. For these reasons, γ-Bi_2MoO_6 has been very popular in the last decade for various types of applications such as photocatalyst [27,28], super capacitor [29], adsorbent [30] and gas sensor [31]. It also has excellent inherent properties like thermal and chemical stability, catalytic and luminescence activity, dielectric nature, low cost, corrosion resistant, and biocompatibility which makes it a good candidate for non-enzymatic sensors [32–35]. Despite this fact, very few research have reported sensors based on Bi_2MoO_6 [36].

The high temperatures (400–700 °C) required for the synthesis of Bi_2MoO_6 via co-precipitation [37] or solid state reaction [38] hamper the control of the product properties such as purity, surface area, grain shape and morphology. Recently hydrothermal and solvothermal methods are mostly used for crystal growth, highly pure and uniform nano material at low temperature [39]. Thus, it can be said that hydrothermal method is a reliable way for the synthesis of nanostructures with various morphologies, high crystallinity, high surface to volume ratio and permeability [40]. Many factors like time [41], temperature [42], pH of solutions [43] and type of surfactant [44] are affective in growth and formation of particles in hydrothermal method. As a result, a variable structure with better catalytic properties can be achieved by design of growth and particle accumulation. In fact it should be considered that shortcomings, such as expensive surfactants and duplicate synthesis methods, restrict the creation of diverse structures [45]. Previously, our research group investigated the effect of amino acids as both functional group additives and self-controlled pH on the synthesis of nine new forms of ZnO which were applied for non-enzymatic detection of glucose [16].

Regrettably, in electrochemical reactions, nano metal oxides lose their reversibility of the redox reaction due to the decrease of conductivity, because of particles agglomeration during the detection process [46]. Resolving this problem increased attention to supporting materials like graphene. Graphene with two dimensional structure, sp^2 carbon hybridization, exceptional properties such as high electron transfer capacity, good conductivity, enormous surface for linking with nanostructures, and great mechanical stability makes it a suitable support to improve nanostructures' properties [47,48]. Consequently, presence of graphene, not only prevents nano metal oxides agglomeration but also improves synergic effect and other properties in sensors performance [46].

Rare reports are based on enzymeless detection of glucose by mixed metal oxide electrocatalysts to benefit the synergetic effect of the two components. Synthesis of the pure single phase of the mixed metal oxides with different morphologies has been always a challenge.

In this work, synthesis of pure phase of bismuth molybdate (BM) become possible by changing of effective factors like pH, temperature and new additives. In order to design different morphologies with or without using dodecylamine (DDA) and cysteine (Cys), three sensors (bullet (BM-C), candy (BM-2DDA) and confetti (BM-2Cys)) were obtained. Thanks to its NH_2, COOH, and SH functional groups, cysteine has enormous coordination affinity to inorganic and metal ions. In addition, self-assembly property of this amino acid can lead to a variety of morphologies for Pb and MoS_2 associations [49,50]. Also there is no report based on the synthesis of -γBi_2MoO_6 by cysteine and dodecylamine assistance. As the best of our knowledge, no research concerns the detection of glucose based on different shapes of γ–Bi_2MoO_6. Finally, bismuth molybdate was mixed and physically with reduced graphene. For the electrochemical experiments, cheap glassy carbon electrodes were employed as glucose sensor. Thus, the expensive gold electrode, Nafion and other stabilizer or conductive materials that are widely used in many sensors, are not utilized. The obtained results displayed outstanding sensitivity and low detection limit. Moreover, glucose selectivity was significant in presence of uric acid, ascorbic acid, dopamine and fructose.

Table 1
Experiment, samples synthesis and achieved morphology conditions.

Product name	Temperature	Time (h)	pH	Additive	Shape
BM-A	140 °C	10	5.8	….	
BM-B	160 °C	10	5.8	….	
BM-C	180 °C	10	5.8	….	**Bullet**
BM-0.5Cys	180 °C	10	4.7	L-Cysteine (0.5 mmol)	
BM-1Cys	180 °C	10	4.4	L-Cysteine (1 mmol)	
BM-2Cys	180 °C	10	4.3	L-Cysteine (2 mmol)	**Confetti**
BM-1DDA	180 °C	10	5	Dodecyl amine (1 mmol)	
BM-2DDA	180 °C	10	5.1	Dodecyl amine (2 mmol)	**Candy**

2. Experimental section

2.1. Apparatus and reagents

Purchased $Bi(NO_3)_3.5H_2O$ (A. R. grade), $Na_2MoO_4.2H_2O$ (A. R. grade), absolute ethanol, L-cysteine and dodecylamine, D-(+)-glucose monohydrate, fructose, dopamine, L-ascorbic acid, uric acid, graphite, sodium nitrate, potassium permanganate, hydrazine monohydrate, hydrogen peroxide, and dimethylformamide were used as received. NaH_2PO_4 and Na_2HPO_4 were used to prepare phosphate buffer solution (PBS). All solutions were prepared using ultra-purified water (>18 MΩc cm) refined by a cartridge purification system (Millipore, UK). The electrochemical measurements were carried out by Metrohm Aoutolab-state-100.

2.2. Instrumentation

Microscopic analysis of samples was performed by field-emission scanning electron microscopy (FESEM) (Sigma VP, ZEISS). X-ray diffractometer (XRD) (X' Pert Pro, Panalytical) with CuKα radiation at 40 kV and 30 mA scanning over 2θ range from 10 to 80° at a rate of 1°/min. Fourier transformed infrared spectroscopy (FT-IR) spectra were recorded using Thermo Scientific Nicolet IS 50 FT-IR spectrometer using KBr disk.

2.3. Preparation of –γBi_2MoO_6

$Na_2MoO_4.2H_2O$ (0.2420 g, 1 mmol; solution A) and $Bi(NO_3)_3.5H_2O$ (0.9702 g, 2 mmol; solution B) were dissolved separately in 35 mL deionized water and stirred in room temperature for 20 min. Solution (A) was added dropwise to solution (B) and stirred for 30 min. The resulting yellow suspension was transferred into 100 mL stainless steel teflon-lined autoclave for 10 h at different temperatures (140, 160 and 180 °C). Precipitate was collected, washed with H2O and EtOH several times, and heated under air to 500 °C for 2 h at the heating rate of 5 °C/min. The obtained yellow powders were named BM-A, BM-B and BM-C, respectively according to the above mentioned temperatures.

To investigate the effect of additives, cysteine (0.5, 1 or 2 mmol) and dodecylamine (1 or 2 mmol) were separately added to solution A and stirred for 10 min. Solution A dropwise was poured into solution B and stirred for 30 min. Then the suspensions were transferred into 100 mL stainless steel teflon-lined autoclave at 180 °C for 10 h. Then all precipitates washed with H_2O and EtOH. Subsequent calcination at 600 °C for 2 h with a heating rate of 5 °C/min afforded yellow powders. They are named BM-0.5Cys, BM-1Cys, BM-2Cys, BM-1DDA and BM-2DDA, respectively. All synthesized compounds and their properties are collected in Table 1.

2.4. Preparation of reduced graphene oxide (rGO)

According to improved hummer method [51], graphite (0.5 g) was

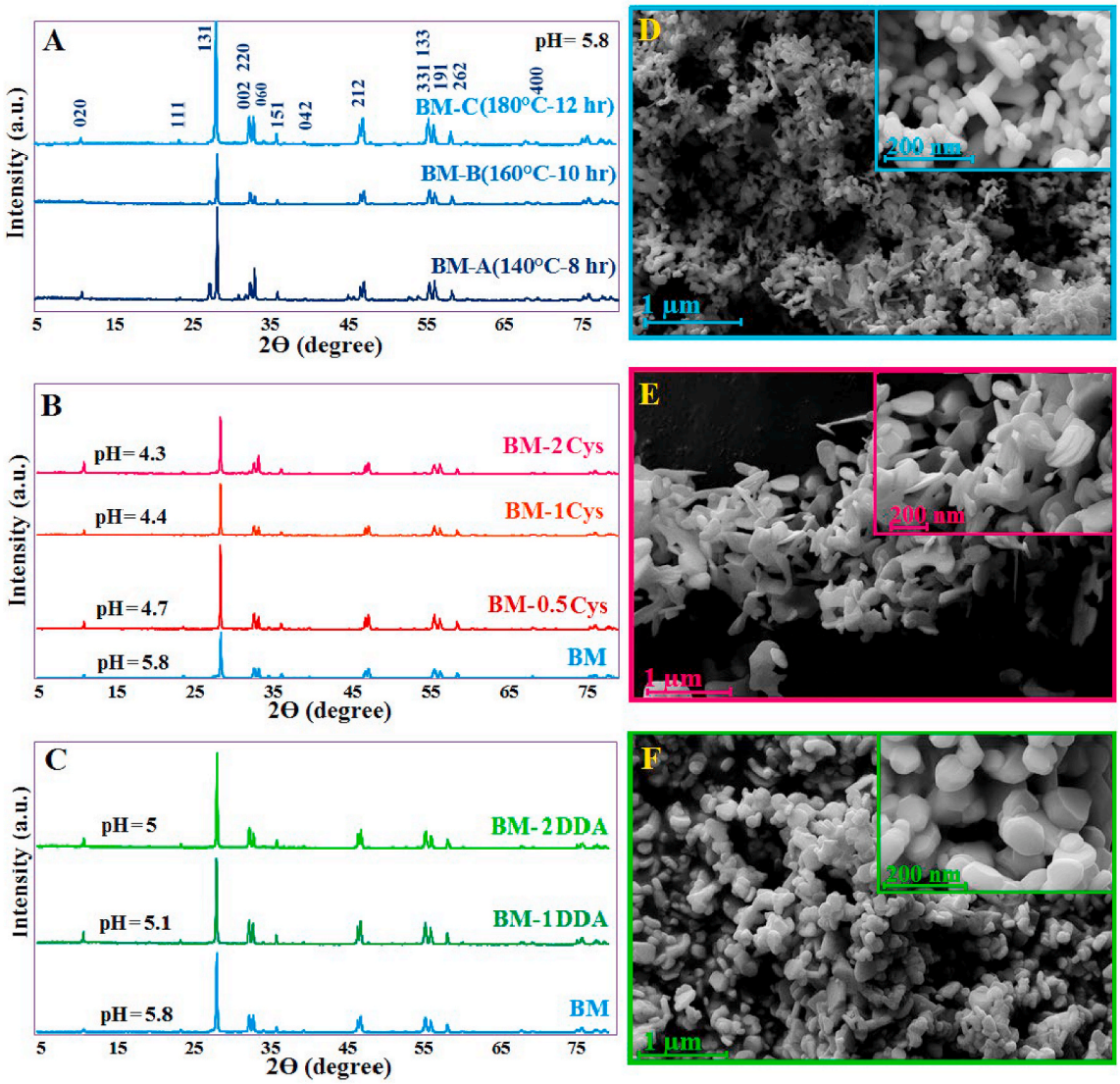

Fig. 1. (A) XRD pattern of all synthesis steps of pure γ-Bi_2MoO_6 after calcination in 550 °C (pH = 5.8) (B) XRD pattern of (BM), (BM-0.5Cys), (BM-1Cys (and (BM-2Cys). (C) XRD pattern of (BM), (BM-1DDA) and (BM-2DDA). FE-SEM micrograph of (D) BM-C (bullet like), (E) BM-2Cys (confetti like) and (F) BM-2DDA (candy like).

mixed with concentrated sulfuric acid (98%, 50 mL). Sodium nitrate (0.5 g, 5 mmol) and potassium permanganate (3 g, 1.8 mmol) were gradually added (15 min) at 0 °C under stirring. Then the solution was stirred at 35 °C for 2 h until it turned to green. After addition of deionized water (200 mL) following by heating to 95 °C, the mixture turned into brown. After cooling to 50 °C, hydrogen peroxide (3 mL) was added. The precipitate was collected, was washed with hydrochloric acid and deionized water for several times, sonicated and dried to form graphene oxide plates. Graphene oxide (0.5 g) was sonicated in dimethylformamide (20 mL). Hydrazine hydroxide (5 mL) was added and the mixture was stirred at 80 °C for 12 h. The sample washed with deionized water and then dried at 60 °C [52].

2.5. Fabrication of Bi_2MoO_6/rGO/GCE modified electrodes

The five calcined samples (BM-0.5Cys, BM-1Cys, BM-2Cys, BM-1DDA and BM-2DDA) (0.3 g) were separately dissolved in deionized water (10 mL) and dimethylformamide (DMF) (10 mL). Afterwards rGO (0.1 g) was added to the solution, sonicated and stirred for 24 h. The black suspension washed with deionized water and EtOH several times and dried at 80 °C. The obtained powder (5 mg) was sonicated in DMF (2 mL) for 1 h and then stirred for 24 h. A withdrawed sample (10 µL) was deposited on electrode and dried at room temperature. The electrode is prepared for electrochemical experiments. The procedure was done for all the five above mentions samples correspondingly for glucose electrochemical measurements.

2.6. Preparation of simulated body fluid (SBF)

SBF was prepared by dissolving $CaCl_2$ (0.278 g), NaCl (7.996 g), KCl (0.224 g), $K_2HPO_4.3H_2O$ (0.228 g), $NaHCO_3$ (0.350 g), $MgCl_2.6H_2O$ (0.305 g), Na_2SO_4 (0.071 g), $H_2NC(CH_2OH)_3$ (6.057 g) and HCl 1 N (40 mL) in 1000 mL deionized water at 37 °C [53].

2.7. Characterization and electrochemical measurements of the electrode

All electrochemical measurements were carried out with three electrode setups at 25 ± 2 °C. A platinum electrode was used as counter and Ag/AgCl was used as reference electrode. The modified GCEs were studied as working electrodes. To cleaning of GCE surface from any environmental contamination, it was brushed in alumina and ethanol grout followed by washing with acetone then it was cycled in the range

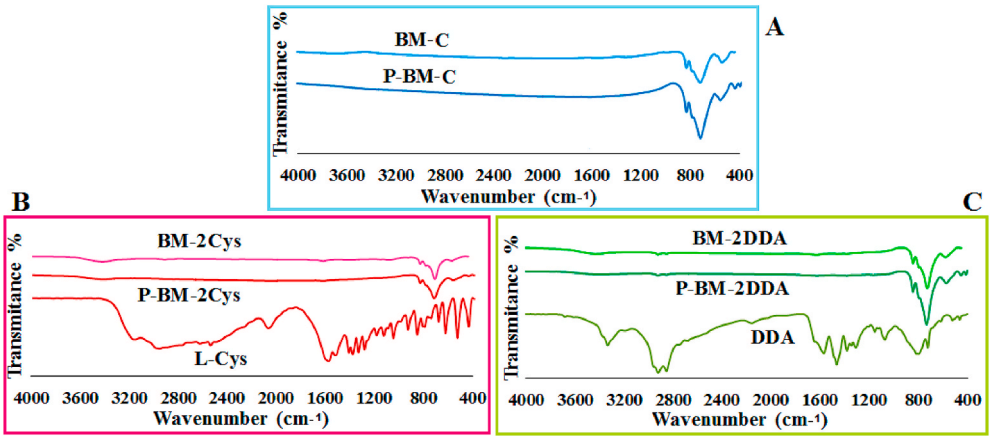

Fig. 2. FT-IR spectrum of (A) Before and after calcination of BM-C, (B) Pure L-cysteine, before and after calcination of BM-2Cys, (C) Pure dodecylamine, before and after calcination of BM-2DDA.

between −1.5 and + 1.5 V (vs. Ag/AgCl), in 5 mmol L^{-1} ferri/ferro solution ($Fe(CN)_6^{3-/4-}$). This is a routine way for pre-cleaning of electrode surface. As well as cyclic voltammetry measurements (CV) and electrochemical impedance spectra (EIS) of electrodes recorded in the Ferri/Ferrocyanide redox probe. Next, the modified electrodes were tested in PBS solution.

Voltage range CV of was between −1.5 and + 1.5 V at scan rate of 50 mV s^{-1} (5 cycles) in different glucose solutions (0.1–1 mmol L^{-1}). Also the chronoamperograms were recorded at +0.17 V potential in every 60 s at 0.02 mmol L^{-1} concentration. 0.05 mmol L^{-1} dopamine (DA), ascorbic acid (AA), uric acid (UA), fructose and 0.1 mmol L^{-1} glucose were added to buffer phosphate solution for the interference test. Finally, stability and repeatability test carried out in 1 mmol L^{-1} glucose solution for best resulted biosensor (BM-2DDA/rGO/GCE) within 8 consecutive weeks. Also for real sample testing, SBF used for negative control. For positive control, 50 μL of glucose with specific concentration was added to SBF every 60 s.

3. Results and discussion

3.1. Structure and morphology characterization

The preparation steps of pure γ-Bi_2MoO_6 powder (BM) was demonstrated in Fig. 1A. In the first step, temperature of the reaction was 140 °C for 10 h. In this sample γ-Bi_2O_3 phase-related impurity was observed at 2θ = 27°. Then, temperature reached to 160 °C which caused a decrease in impurities. At the final step, temperature increased to 180 °C. As can be seen from Fig. 1A, there is no extra impurity patterns which proves our simple synthesis method for pure phase of γ-Bi_2MoO_6. All observations approved that all peaks are related to orthorhombic phase of bismuth molybdate (JCPDS no. of 21–0102, a = 5.502 Å, b = 16.213 Å and c = 5.483 Å) [54]. It can be concluded that impurity peaks are related to accidental and irregular presence of Bi_2O_3 crooked shape fluorite in MoO_4 plates which disappear by the increase of temperature and reaction time. Gradually, MoO_4^{-2} formed and island like $L-Bi_{2n+4}Mo_nO_{6(n+1)}$pieces shaped by gathering together and assisting the construction of γ-Bi_2MoO_6. Finally, at high temperature, the rate of nucleation increases, and particles easily start shaping and growing.

Fig. 1 represents FE-SEM images. Fig. 1D showed a bullet like morphology. As samples were synthesized in near neutral pH, acidic properties decreased (Table 1). As a result, acidic protons will collect on {100} and {001} facets. In these facets the energy levels and oxygen density reduce. Finally, the growth of particles may take place in vertical or rod shapes in {010} facet [26]. The effect of L-cysteine additive's concentration on surface growth was demonstrated in Fig. 1B. By increasing the amount of cysteine, the intensity of (060), (212) and (020) planes in BM-2Cys increases in comparison with BM, whereas the intensity of (131) plane decreases. According to FE-SEM image in Fig. 1E, confetti morphology was formed. On the other hand, Table 1 shows that the pH of solutions is acidic (~4) and the presence of abundant amount of H^+ on {010} facet leads to adsorption of oxygens, which decreases the energy of this surface [55]. Therefore, the vertical growth in this plane is stopping and leads to form plate like morphology in {001} and {100} surfaces. Fig. 1C shows that the intensity of (331), (002) and (131) diffractions in 2 mmol dodecylamine compound (BM-2DDA) increases and forms multidimensional morphology which is slightly wider than rod and semi candy-like (Fig. 1F). In the presence of dodecylamine, Bi^{+3} can only coordinate to amine group. According to Table 1 this compound's pH is less acidic than pH of cysteine's solution, so the growth of structures in all {100}, {001} and {010} surfaces is possible. According to some recent research, the presence of dodecylamine leads to the sphere-like morphology of metal oxides [56,57].

FT-IR spectra (Fig. 2) shows various synthesized bismuth molybdate samples. Fig. 2A concerns the pre calcined BM-C (P-BM-C) sample which is synthesized at 180 °C for 10 h and BM-C which was calcined at 550 °C for elimination of impurities. Small and wide peak in 3419 cm^{-1} is related to stretching vibration of O-H group. Two peaks around 844 and 780 cm^{-1} are related to MoO_6's symmetric and asymmetric vibration of axial oxygen atoms, respectively. A very sharp peak at 729 cm^{-1} is related to asymmetric stretching of equatorial oxygen atoms in MoO_6 and also bending vibration of MoO_6 can be observed at 555 cm^{-1}. The stretching and bending vibrations of BiO_6 were indicated as a small peak around 457 cm^{-1} [58,59]. Fig. 2B is related to the bismuth molybdate synthesized with L-cysteine (2 mmol) assistance; it is shown as pre calcined BM-2Cys (P-BM-2Cys) and BM-2Cys after calcination at 600 °C for removing of cysteine. In FT-IR spectra of cysteine, 1532 and 1580 cm^{-1} vibrations correspond to single and double bonds of the amino acid. These vibrations are shifted to 1626 and 1719 cm^{-1} in P-BM-2Cys and BM-2Cys compounds that are related to single and double bonds of acyl amine group (-CO-NH_2-), respectively with weak intensity which is almost disappeared. The peak of N-H at 2080 cm^{-1} and the sharp peak of S-H at 2549 cm^{-1} are also disappeared. The growth mechanism and crystalline orientation of the compound proved that S-H and N-H functional groups have great tendency to link to Bi metal ion [60]. Three FT-IR spectra in Fig. 2C are related to dodecylamine (DDA), bismuth molybdate synthesized with 2 mmol dodecylamine before calcination (P-BM-2DDA) and the calcined form of it at 600 °C (BM-2DDA). 2853 and 2919 cm^{-1} vibrations in DDA are relevant to stretching of C-H band, while the sharp peak at 3330 cm^{-1} is assigned to N-H (amine) group which is completely faded in (P-BM-2 DDA) [61]. 1381 and 1464 cm^{-1} peaks are relevant to CH_3 and CH_2 bending vibrations, which are

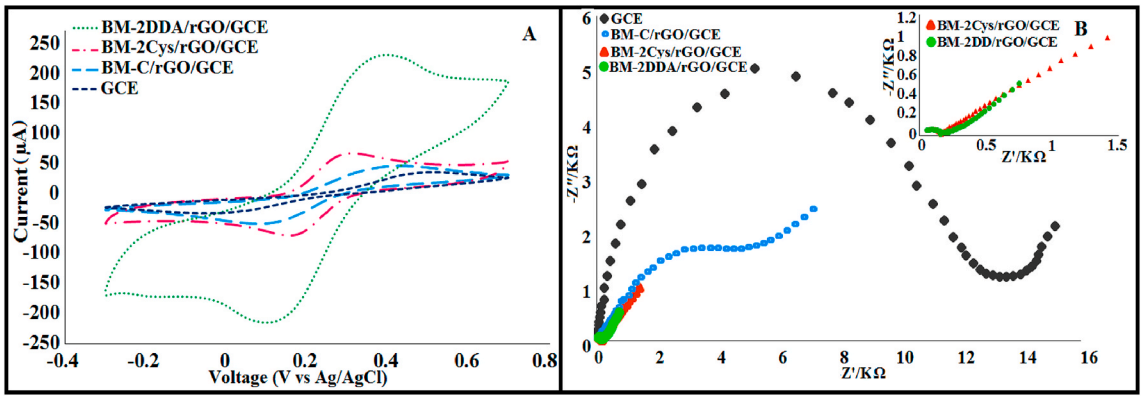

Fig. 3. (A) CVs and (B) Nyquist plots of the GCE, BM-C/rGO/GCE, BM-2Cys/rGO/GCE and BM-2DDA/rGO/GCE in 5 mmol L^{-1} $Fe(CN)_6^{3-/4-}$ solution.

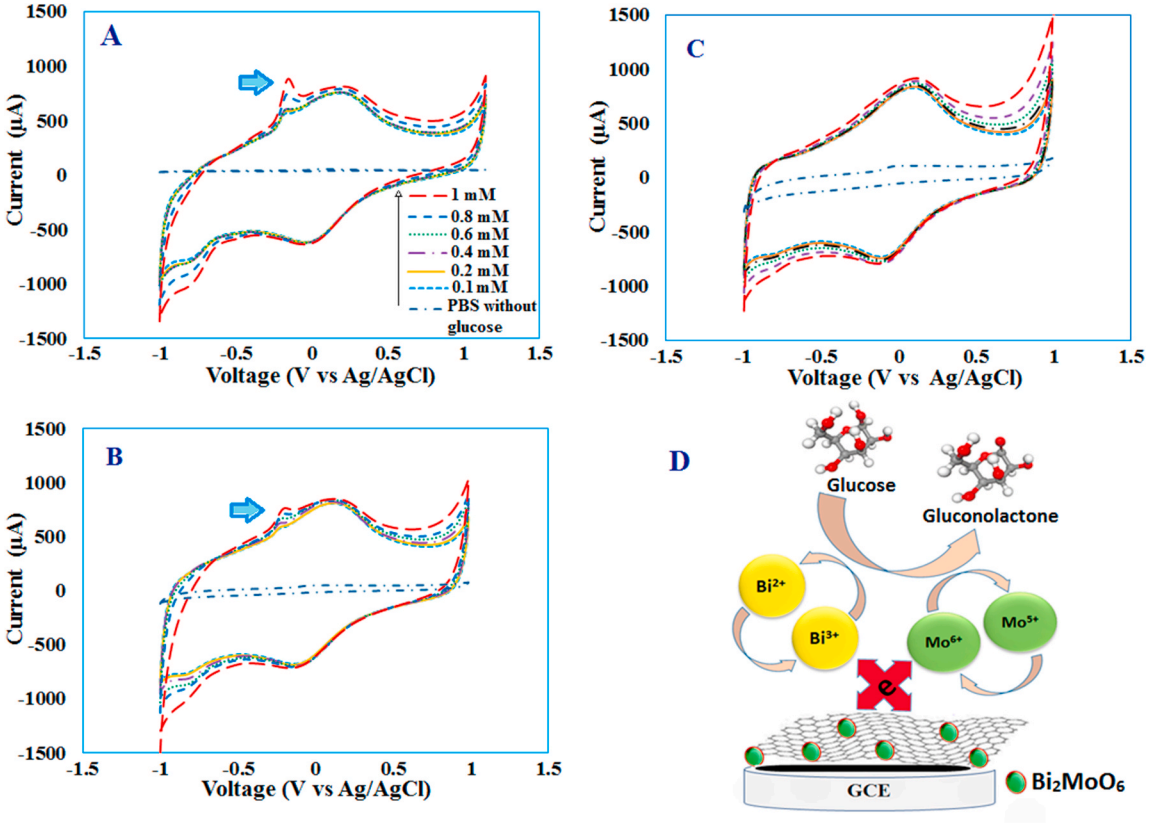

Fig. 4. Typical CV curve of electrodes. All CV was done in PBS solution with 0.1–1 mmol L^{-1} concentration of glucose and absence of it with scan rate 50 mV s^{-1} (A) BM-A, (B) BM-B and (C) BM-C. (D) Schematic representation of the electrocatalytic oxidation mechanism of glucose at Bi_2MoO_6 modified GCEs.

weakly, appeared in P-BM-2DDA. It can be concluded that at high temperature (after calcination at 600 °C), dodecylamine and L-cysteine (organic additives) are excluded because of the lack of related vibrational peaks.

3.2. Characterization of different electrodes by CV and EIS

To evaluate the different electrodes, a 5 mmol L^{-1} $Fe(CN)_6^{3-/4-}$ solution was used as electrochemical probe. The electrochemical behavior of the probe was investigated at the surface of bare GCE, BM-C/rGO/GCE, BM-2Cys/rGO/GCE and BM-2DDA/rGO/GCE using CV method (Fig. 3A). The separation of the oxidation and reduction peak potentials in the ferri/ferro solution at the surface of GCE was 480 mV representing that the conversion of Fe^{2+} to Fe^{3+} is slow. However, the oxidation-reduction peaks current of the probe at the surface of BM-C/rGO/GCE, BM-2Cys/rGO/GCE and BM-2DDA/rGO/GCE were higher than the surface of GCE, as well the potential difference between the redox peaks was fewer than bare GCE, which indicate reversible reaction. The EIS was applied as a powerful method to investigate the improvement of the electrochemical behavior of the GCE toward the used probe during different steps of modification by comparing the electron transfer resistance (R_{ct}) given from the semicircle parts of obtained curves [62]. According to Fig. 3B, the values of R_{ct} at the surfaces of bare GCE, BM-C/rGO/GCE, BM-2Cys/rGO/GCE and BM-2DDA/rGO/GCE resulted from the Nyquist plots were 13.32 (±0.05), 5.24 (±0.03), 0.19 (±0.03) and 0.18 (±0.01) KΩ, respectively. The decreased values at the surface of BM-C/rGO/GCE, BM-2Cys/rGO/GCE and BM-2DDA/rGO/GCE in compare with bare GCE is resulted from the synergetic effect of

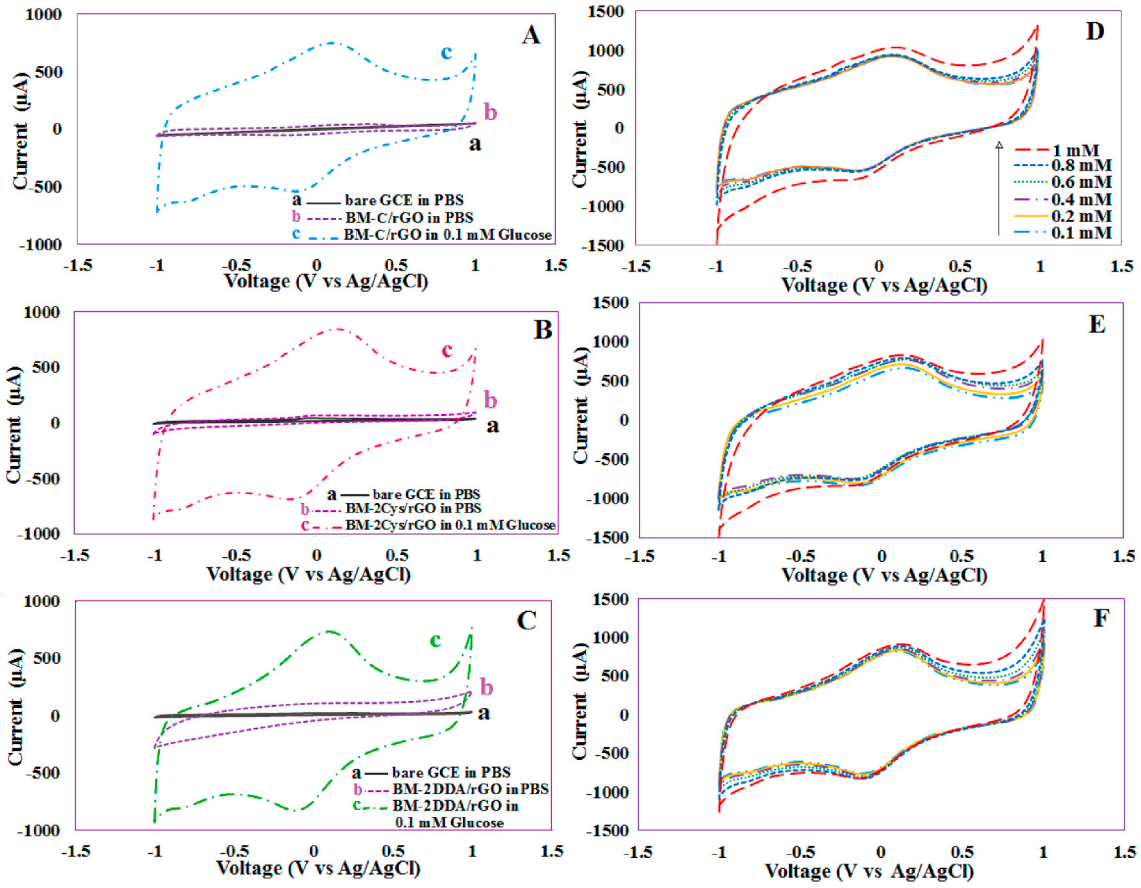

Fig. 5. CV of (A) simple GCE in PBS, BM-C/rGO/GCE in PBS and BM-C/rGO/GCE in 0.1 mmol L^{-1} glucose for the samples, (B) simple GCE in PBS, BM-2Cys/rGO/GCE in PBS and BM-2Cys/rGO/GCE in 0.1 mmol L^{-1} glucose for the samples and (C) simple GCE in PBS, BM-2DDA/rGO/GCE in PBS and BM-2DDA/rGO/GCE in 0.1 mM glucose for the samples. Different concentrations of glucose 0.1–1 mmol L^{-1} for (D) BM-C/rGO/GCE, (E) BM-2Cys/rGO/GCE and (F) BM-2DDA/rGO/GCE.

nanoparticles and reduced graphene oxide, which cause increasing the electron transfer rate.

3.3. Electrochemical behavior of the modified electrodes

All electrochemical experiments were done in buffer phosphate and CVs were measured in the voltage range of ±1.5 V. In Fig. 4 the CVs illustrate the purification steps of bismuth molybdates at different temperatures. Fig. 4A corresponds to the synthesis of BM-A/rGO/GCE at 140 °C for 10 h, which is combined simply and physically with graphene, then deposited on GCE. The modified electrode firstly was tested in PBS, then measured between 0.1 and 1 mmol L^{-1} concentrations of glucose.

Based on the XRD analyses of Fig. 1A, a great amount of Bi_2O_3 impurities exists. As a result, two oxidation peaks in CV are related to Bi_2MoO_6 and Bi_2O_3 at +0.17 and −0.2 V, respectively. Fig. 4B shows the CV of BM-B/rGO/GCE synthesized at 160 °C for 10 h; the second sharp peak which is related to Bi_2O_3 is slightly reduced in −0.2 V while the intensity of the first peak remains constant.

Fig. 4C is related to a pure single phase of Bi_2MoO_6 synthesized at 180 °C for 10 h which was combined with graphene and incorporated on electrode (BM-C/rGO/GCE). According to XRD pattern (Fig. 1A), Bi_2O_3 impurity is removed. Therefore, only pure phase played the oxidation and reduction on the surface of electrode (Fig. 4C). Increasing the synthesis temperature of pure bismuth molybdate leads to fading of the oxidation peak in negative region.

As we could not find any research about glucose identification by bismuth molybdate, considering evidences and studies for other sensors and interesting catalytic properties of this structure, a hypothesis can be proposed that glucose identification in specific voltage region can be observed. Fig. 4D illustrates schematic representation of the electrocatalytic oxidation mechanism of glucose at Bi_2MoO_6 modified GCEs. According to electrochemical behavior of γ-Bi_2MoO_6 [63], distribution of oxygen network plays an important role in oxidation reaction and its redox reaction is considerably different from the metal oxides, so the peak point at high positive voltage region is related to γ-Bi_2MoO_6. According to predictions, a Bi-O^{-2} is replaced with nearest Mo-O^{-2} bond and after that, oxygen vacancy is filled. On the other hand, in electrocatalytic activity of molybdenum oxide recorded by Density Functional Theory (DFT) analyses it was proved that electron transportation takes place from glucose oxygen's p orbital to molybdenum's d orbital which are in the nearest position to each other [7,63].

Triple peaks in Fig. 5 A, B and C also demonstrate the glucose identification by (BM-C/rGO/GCE), (BM-2Cys/rGO/GCE) and (BM-2DDA/rGO/GCE) biosensors. As an example, Fig. 4A is related to bullet morphology. At first, bare electrode was tested in buffer phosphate solution (pH = 7) and then the modified electrode combined with (BM-C/rGO/GCE) sensor tested by CV in PBS solution and in the absence of glucose. In final step, biosensor was tested in solution containing 0.1 mmol L^{-1} glucose. We found the interesting fact that in the presence of glucose, electrooxidation capability increased in the sensor. Besides the oxidation peak increased considerably in absence of glucose. So CV curves were similar to bare electrode in PBS and a nominal redox is observed. These two steps were repeated for two other biosensors with confetti and candy-like morphologies (Fig. 5B and C). Therefore, considerable increase in oxidation-reduction peak is observed in all three Figures, due to increase of glucose concentration in solution. The connection between different concentrations of glucose in electrolyte

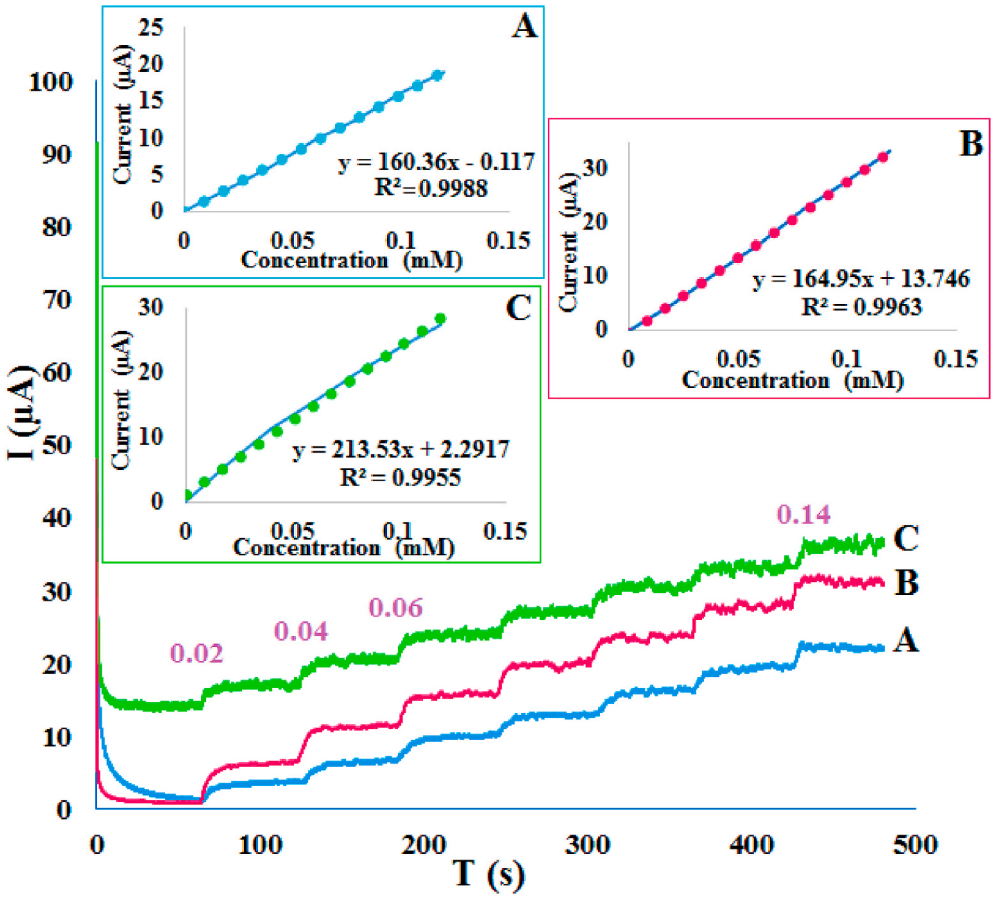

Fig. 6. Chronoamperomograms of 3 sensors (A) BM-C/rGO/GCE, (B) BM-2Cys/rGO/GCE and (C) BM-2DDA/rGO/GCE and their calibration curves.

Table 2
Performance comparison of the glucose sensors in this work with other literatures.

Electrode composition	Type of biosensor	Sensitivity (μA L mmol^{-1} cm^{-2})	Detection limit (mmol L^{-1})	Linear range (mmol L^{-1})	year	Ref
p-NiO/n-$Bi_4Ti_3O_{12}$	Enzymatic	215	0.001	0.02–3.55	2018	[64]
$BiVO_4$	Non-enzymatic	….	0.0001	0–5	2019	[6]
HO-$BiONO_3$	Non-enzymatic	8.2×10^2	0.0001	0.005–2.1	2016	[65]
BiOCl/TiO_2	Non-enzymatic	0.417	0.0057	0–1.3	2014	[66]
MoO_3	Non-enzymatic	15.4	0.005–0.175	…	2017	[7]
MoS_2-$NiCo_2O_4$	Non-enzymatic	1748.58	0.00015	0.001–11.1	2017	[67]
MoS_2-CuS	Non-enzymatic	…	0.0003	0.001–0.1	2017	[68]
Au-Pd/MoS_2	Non-enzymatic	184.9	0.40	0.5–20	2017	[69]
Ni-MoS_2/rGO	Non-enzymatic	256.1	0.00015	0.005–8.2	2017	[70]
BM-C/rGO/GCE	Non-enzymatic	2290	0.006	0.02–0.14	2019	This work
BM-2Cys/rGO/GCE	Non-enzymatic	2356	0.006	0.02–0.14	2019	This work
BM-2DDA/rGO/GCE	Non-enzymatic	3050	0.004	0.02–0.14	2019	This work

and the intensity of peaks was investigated in CV charts (Fig. 5). Glucose concentration between 0.1 and 1 mmol L^{-1} for all (BM-C/rGO/GCE), (BM-2Cys/rGO/GCE) and (BM-2DDA/rGO/GCE) biosensors can be observed in Fig. 5D, E and F. An excellent performance for direct oxidation of glucose was noted: clear increase of the current for a slight increase in glucose amount.

3.4. Amperometric detection of glucose

Amperometric i-t curves in optimized constant voltage (+0.17 V) and optimized rmp stirring (115) with scan rate of 50 mV s^{-1} were recorded to determine the sensitivities (Fig. 6). The current responses of amperometric i–t curves increase with the glucose concentration. As can be seen in the chronoamperomograms, current was increased after addition of the lowest amount of glucose (0.02 mmol L^{-1}) into the 0.1 mol L^{-1} PBS solution in every 60 s. For all three sensors of BM-C/rGO/GCE, BM-2Cys/rGO/GCE and BM-2DDA/rGO/GCE, standard calibration curve from the lowest to the highest concentration of glucose (0.02–0.14 mmol L^{-1}) was plotted and a very exact line equation and curve slope were obtained (Fig. 6A, B and C). Moreover, detection limit and sensitivity with S/N = 3 for these biosensors were calculated (Table 2). In this study, γ-Bi_2MoO_6 is reported as a non-enzymatic glucose biosensor for the first time. Fortunately, in comparison with other research reports of other existed sensory materials, which were illustrated in Table 2 along with our results, γ-Bi_2MoO_6 revealed very good sensitivities (2290, 2356 and 3050 μA mM^{-1} cm^{-2} for BM-C/rGO/GCE, BM-2Cys/rGO/GCE and BM-2DDA/rGO/GCE, respectively).

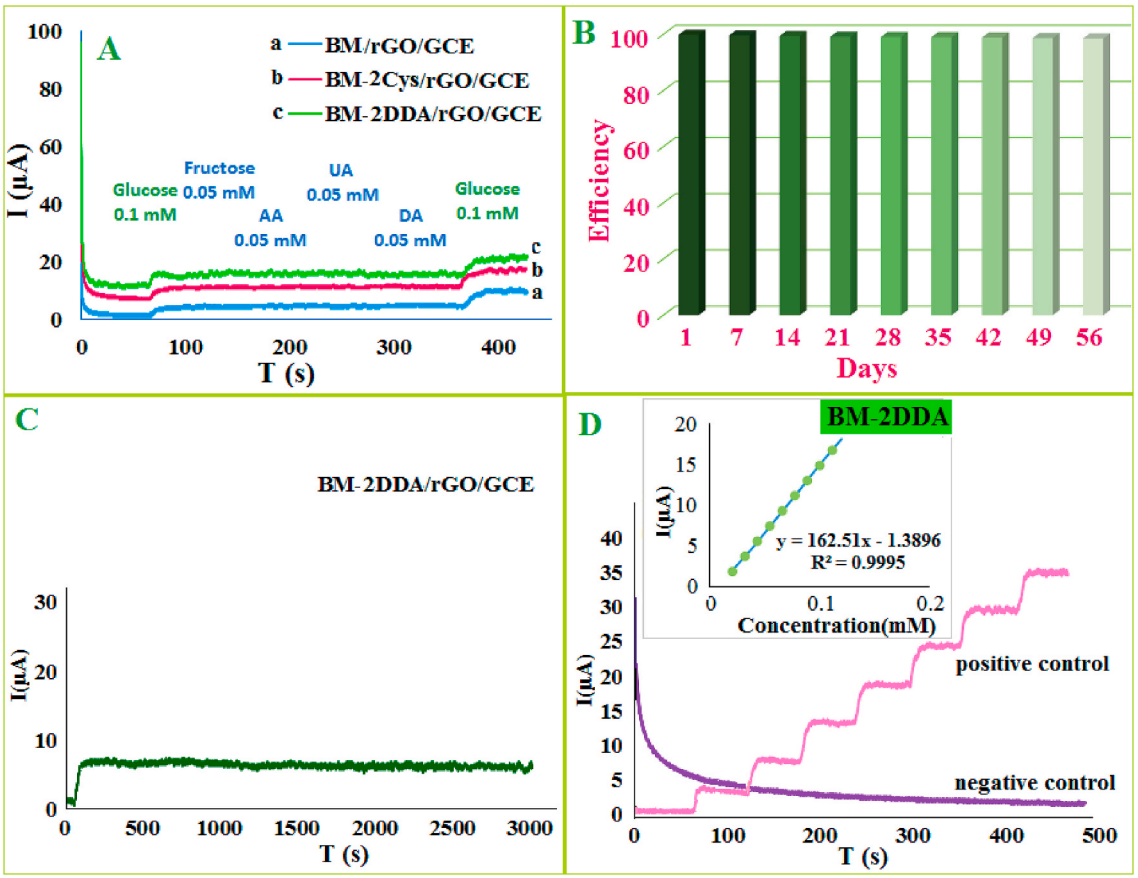

Fig. 7. (A) Amperometric selective responses of BM-C/rGO/GCE, BM-2Cys/rGO/GCE and BM-2DDA/rGO/GCE at +0.17 V with 0.1 mmol L^{-1} glucose and other electroactive biomolecules including 0.05 mmol L^{-1} AA, UA, dopamine and fructose in PBS, (B) Stability of BM-2DDA/rGO/GCE in its continuous use for 8 weeks towards 0.02 mmol L^{-1} glucose in 0.1 mol L^{-1} PBS, (C) Prolonged amperometric response of BM-2DDA/rGO/GCE to the presences of 0.02 mmol L^{-1} glucose in 0.1 mol L^{-1} PBS for 3000s, (D) The reliability test for BM-2DDA/rGO/GCE glucose biosensor in SBF.

3.5. Selectivity toward glucose

Interfering test is an important issue for non-enzymatic electrochemical glucose sensors. 0.5 mmol L^{-1} concentration of ascorbic acid (AA), uric acid (UA), dopamine (DA) and fructose solutions were made, and in constant voltage of +0.17 V and specified time, were added to the buffer phosphate solution. Furthermore, 0.1 mmol L^{-1} glucose solution was added to the PBS solution in first and last step of this investigation (Fig. 7A). According to the three charts of Fig. 7A, no response of interfering species is noticeable and the sensitivity of sensors among other biomolecules about glucose sensing is very impressive. As mentioned before, among all three final compounds, BM-2DDA/rGO/GCE with candy like morphology showed better sensitivity (3050 μA L $mmol^{-1}$ cm^{-2}). According to the results, the best performance is achieved by altering to semi sphere morphology [16]. Thus, stability and repeatability tests were done on the above mentioned best biosensor.

3.6. The repeatability, reproducibility, stability of BM-2DDA/rGO/GCE sensor

Repeatability refers to precision of a sample by successive measurements, whereas reproducibility demonstrates the closeness of the results, using the same method under various conditions (different electrodes) [16,71].

Repeatability of (BM-2DDA/rGO/GCE) biosensor consecutively measured 12 times in one day with 0.1 mmol L^{-1} glucose concentration and relative standard deviation of RSD = 1.67% was achieved. Moreover, reproducibility was tested with five different (BM-2DDA/rGO/GCE) electrodes in 0.1 mmol L^{-1} glucose concentration and showed very low RSD equal to 2.21%.

Stability is a necessary feature for all kinds of biosensors, stability and half-life of (BM-2DDA/rGO/GCE) electrode was investigated in 8 weeks with glucose concentration of 0.02 mmol L^{-1} (Fig. 7B). The modified electrode was kept at room temperature and away from moisture within this time. They showed maintenance of (99.65%) and (98.51%) of their early response after 7 and 56 days, respectively. Although the electrode is modified with a simple physical adsorption method, it showed a long-term stability and durability in comparison to reports which used expensive materials like Nafion and PVP [72].

In order to Fig. 7C shows the current response of BM-2DDA/rGO/GCE for a large period of time after adding 0.02 mmol L^{-1} of the analyte. It can be seen that after 50 min, the sensor represented only 7% decrease in current. This small decrease in sensor response may be related to the decrease in glucose concentration decomposed by constant potential electrolysis.

3.7. Reliability as biosensor in real sample

Simulated body fluids (SBF, pH = 7) were used for testing the real application of electrode [53]. At first step SBF sample is used as a negative control. The current increase is noticeable with adding a constant amount of glucose to solution for positive control (Fig. 7D). In addition, even in the presence of different salts in simulated blood serum, no interruption occurred in sensing of glucose. All observations led to suitability of the (BM-2DDA/rGO/GCE) electrode as a simple, non-enzymatic and cheap biosensor in the real sample.

4. Conclusions

In summary, three pure γ-Bi_2MoO_6 mixed metal oxides were synthesized with bullet, confetti and candy-like morphologies using hydrothermal method with/without L-cysteine and dodecylamine additives. A mixture of each of these compounds with reduced graphene oxide was deposited on three electrodes and at the end, three non-enzymatic glucose biosensors of BM-C/rGO/GCE, BM-2Cys/rGO/GCE and BM-2DDA/rGO/GCE with were prepared and showed great applications. In addition, these biosensors have a high selectivity toward glucose even in the presence of ascorbic acid (AA), uric acid (UA), dopamine or fructose. Best sensitivity of 3050 μA L $mmol^{-1}$ cm^{-2} with 0.02–0.14 mmol L^{-1} linear range was calculated for BM-2DDA/rGO/GCE biosensor at +0.17 V in PBS, which fortunately showed lower electron transfer resistance, perfect repeatability, short response time, suitable stability and reproducibility. Outstanding performance of glucose detection in this biosensor can be attributed to its multidimensional spherical structure. Combination of BM-2DDA/rGO/GCE with graphene plates probably leads to a material allowing the increase of electron transportation speed. The detection of low concentration of glucose (20 μmol L^{-1}) by this probe is very noticeable in comparison with other non-enzymatic glucose sensors. Moreover, the reliability application of biosensor in SBF solution was completely successful. Consequently, and because of the simple synthesis, cheap electrode, no use of stabilizers, PVP, Nafion and glucose oxidase, the design of this system is remarkable for biomolecule sensors, gas sensors and photocatalysts.

Declaration of competing interest

The authors declare that they have no known competing financial interests or personal relationships that could have appeared to influence the work reported in this paper.

Acknowledgment

We thank Chemistry & Chemical Engineering Research Center of Iran (CCERCI) as well as Miss Sommayeh Golsanamlou for her help.

References

[1] C. Sabu, T.K. Henna, V.R. Raphey, K.P. Nivitha, K. Pramod, Advanced biosensors for glucose and insulin, Biosens. Bioelectron. 141 (2019) 111201.
[2] N.S. Ridhuan, K. Abdul Razak, Z. Lockman, Fabrication and characterization of glucose biosensors by using hydrothermally grown ZnO nanorods, Sci. Rep. 8 (2018) 1–12.
[3] K. Ramachandran, T. Raj Kumar, K.J. Babu, G. Gnana Kumar, Ni-Co bimetal nanowires filled multiwalled carbon nanotubes for the highly sensitive and selective non-enzymatic glucose sensor applications, Sci. Rep. 6 (2016) 1–12.
[4] F. Tehrani, B. Bavarian, Facile and scalable disposable sensor based on laser engraved graphene for electrochemical detection of glucose, Sci. Rep. 6 (2016) 1–10.
[5] P. Saeedi, P. Salpea, S. Karuranga, I. Petersohn, B. Malanda, E.W. Gregg, N. Unwin, S.H. Wild, R. Williams, Mortality attributable to diabetes in 20–79 years old adults, 2019 estimates: results from the international diabetes federation diabetes atlas, Diabetes Res. Clin. Pract. 2017 (2020) 108086, 9th ed.
[6] S. Wang, S. Li, W. Wang, M. Zhao, J. Liu, H. Feng, Y. Chen, Q. Gu, Y. Du, W. Hao, A non-enzymatic photoelectrochemical glucose sensor based on $BiVO_4$ electrode under visible light, Sensor. Actuator. B Chem. 291 (2019) 34–41.
[7] M. Sharma, A. Gangan, B. Chakraborty, C.S. Rout, Non-enzymatic glucose sensing properties of MoO_3 nanorods: experimental and density functional theory investigations, J. Phys. D Appl. Phys. 50 (2017) 475401.
[8] Y. Li, M. Xie, X. Zhang, Q. Liu, D. Lin, C. Xu, F. Xie, X. Sun, Co-MOF nanosheet array: a high-performance electrochemical sensor for non-enzymatic glucose detection, Sensor. Actuator. B Chem. 278 (2019) 126–132.
[9] C. Shan, H. Yang, J. Song, D. Han, A. Ivaska, L. Niu, Direct electrochemistry of glucose oxidase and biosensing for glucose based on graphene, Anal. Chem. 81 (2009) 2378–2382.
[10] C. Wu, H. Sun, Y. Li, X. Liu, X. Du, X. Wang, P. Xu, Biosensor based on glucose oxidase-nanoporous gold co-catalysis for glucose detection, Biosens. Bioelectron. 66 (2015) 350–355.
[11] S. Park, H. Boo, T.D. Chung, Electrochemical non-enzymatic glucose sensors, Anal. Chim. Acta 556 (2006) 46–57.
[12] W.C. Lee, K.B. Kim, N.G. Gurudatt, K.K. Hussain, C.S. Choi, D.S. Park, Y.B. Shim, Comparison of enzymatic and non-enzymatic glucose sensors based on hierarchical Au-Ni alloy with conductive polymer, Biosens. Bioelectron. 130 (2019) 48–54.
[13] J. Xu, F. Li, D. Wang, M.H. Nawaz, Q. An, D. Han, L. Niu, Co_3O_4 nanostructures on flexible carbon cloth for crystal plane effect of nonenzymatic electrocatalysis for glucose, Biosens. Bioelectron. 123 (2019) 25–29.
[14] L.M. Lu, H.B. Li, F. Qu, X.B. Zhang, G.L. Shen, R.Q. Yu, In situ synthesis of palladium nanoparticle-graphene nanohybrids and their application in nonenzymatic glucose biosensors, Biosens. Bioelectron. 26 (2011) 3500–3504.
[15] R. Li, X. Liu, H. Wang, Y. Wu, Z. Lu, High-performance hybrid electrode decorated by well-aligned nanograss arrays for glucose sensing, Biosens. Bioelectron. 102 (2018) 288–295.
[16] A. Tarlani, M. Fallah, B. Lotfi, A. Khazraei, S. Golsanamlou, J. Muzart, M. Mirza-Aghayan, New ZnO nanostructures as non-enzymatic glucose biosensors, Biosens. Bioelectron. 67 (2015) 601–607.
[17] R. Yuan, H. Li, X. Yin, J. Lu, L. Zhang, 3D CuO nanosheet wrapped nanofilm grown on Cu foil for high-performance non-enzymatic glucose biosensor electrode, Talanta 174 (2017) 514–520.
[18] A. Ashok, A. Kumar, F. Tarlochan, Highly efficient nonenzymatic glucose sensors based on CuO nanoparticles, Appl. Surf. Sci. 481 (2019) 712–722.
[19] S. Mani, V. Vediyappan, S.M. Chen, R. Madhu, V. Pitchaimani, J.Y. Chang, S. Bin Liu, Hydrothermal synthesis of $NiWO_4$ crystals for high performance non-enzymatic glucose biosensors, Sci. Rep. 6 (2016) 2–9.
[20] J. Yang, H. Ye, Z. Zhang, F. Zhao, B. Zeng, Metal–organic framework derived hollow polyhedron $CuCo_2O_4$ functionalized porous graphene for sensitive glucose sensing, Sensor. Actuator. B Chem. 242 (2017) 728–735.
[21] K.K. Naik, A. Gangan, B. Chakraborty, S.K. Nayak, C.S. Rout, Enhanced nonenzymatic glucose-sensing properties of electrodeposited $NiCo_2O_4$-Pd nanosheets: experimental and DFT investigations, ACS Appl. Mater. Interfaces 9 (2017) 23894–23903.
[22] H. Yu, L. Jiang, H. Wang, B. Huang, X. Yuan, J. Huang, J. Zhang, G. Zeng, Modulation of Bi_2MoO_6-based materials for photocatalytic water splitting and environmental application: a critical review, Small (2019), 1901008, 1–30.
[23] Y. Hao, X. Dong, S. Zhai, X. Wang, H. Ma, X. Zhang, Towards understanding the photocatalytic activity enhancement of ordered mesoporous Bi_2MoO_6 crystals prepared via a novel vacuum-assisted nanocasting method, RSC Adv. 6 (2016) 35709–35718.
[24] Z. Jia, F. Lyu, L.C. Zhang, S. Zeng, S.X. Liang, Y.Y. Li, J. Lu, Pt nanoparticles decorated heterostructured g-C_3N_4/Bi_2MoO_6 microplates with highly enhanced photocatalytic activities under visible light, Sci. Rep. 9 (2019) 1–13.
[25] Q. He, Y. Ni, S. Ye, Heterostructured Bi_2O_3/Bi_2MoO_6 nanocomposites: simple construction and enhanced visible-light photocatalytic performance, RSC Adv. 7 (2017) 27089–27099.
[26] Y. Peng, Y. Zhang, F. Tian, J. Zhang, J. Yu, Structure tuning of Bi_2MoO_6 and their enhanced visible light photocatalytic performances, Crit. Rev. Solid State Mater. Sci. 42 (2017) 347–372.
[27] F. Ding, P. Chen, F. Liu, L. Chen, J.-K. Guo, S. Shen, Q. Zhang, L.-H. Meng, C.-T. Au, S.-F. Yin, Bi_2MoO_6/g-C_3N_4 of 0D/2D heterostructure as efficient photocatalyst for selective oxidation of aromatic alkanes, Appl. Surf. Sci. 490 (2019) 102–108.
[28] Y. Pei, X. Li, H. Chu, Y. Ge, P. Dong, R. Baines, L. Pei, M. Ye, J. Shen, Anion-exchange engineering of cookie-like Bi_2S_3/Bi_2MoO_6 heterostructure for enhanced photocatalytic activities and gas-sensing properties, Talanta 165 (2017) 44–51.
[29] J. Yesuraj, S. Austin Suthanthiraraj, O. Padmaraj, Synthesis, characterization and electrochemical performance of DNA-templated Bi_2MoO_6 nanoplates for supercapacitor applications, Mater. Sci. Semicond. Process. 90 (2019) 225–235.
[30] Q. Campbell, D. Fisher, I. Dabo, Voltage-dependent reconstruction of layered Bi_2WO_6 and Bi_2MoO_6 photocatalysts and its influence on charge separation for water splitting, Phys. Rev. Mater. 3 (2019) 1–8.
[31] F. Zhang, X. Dong, X. Cheng, Y. Xu, X. Zhang, L. Huo, Enhanced gas-sensing properties for trimethylamine at low temperature based on MoO_3/$Bi_2Mo_3O_{12}$ hollow microspheres, ACS Appl. Mater. Interfaces 11 (2019) 11755–11762.
[32] G. Tian, Y. Chen, W. Zhou, K. Pan, Y. Dong, C. Tian, H. Fu, Facile solvothermal synthesis of hierarchical flower-like Bi_2MoO_6 hollow spheres as high performance visible-light driven photocatalysts, J. Mater. Chem. 21 (2011) 887–892.
[33] J. Liu, M. Zeng, H. Dong, Y. Wang, X. Liu, R. Yu, J. He, Photocatalytic activity of Fe_3O_4/Bi_2MoO_6 composite in Rhodamine B decomposition, J. Appl. Phys. 117 (2015) 17D709.
[34] J. Di, J. Xia, M. Ji, H. Li, H. Xu, H. Li, R. Chen, The synergistic role of carbon quantum dots for the improved photocatalytic performance of Bi_2MoO_6, Nanoscale 7 (2015) 11433–11443.
[35] L. Wang, Z. Liu, D. Wang, S. Ni, D. Han, W. Wang, L. Niu, Tailoring heterostructured Bi_2MoO_6/Bi_2S_3 nanobelts for highly selective photoelectrochemical analysis of gallic acid at drug level, Biosens. Bioelectron. 94 (2017) 107–114.
[36] F. Zhang, Y. Xu, X. Zhang, L. Sui, P. Hu, Z. Zheng, X. Cheng, S. Gao, H. Zhao, L. Huo, Highly selective ppb-level H 2 S sensor based on the walnut-like Bi_2MoO_6 at low temperature, Sensor. Actuator. B Chem. 277 (2018) 312–319.
[37] L. Banavatu, D.S. Rao, K. Basavaiah, Synthesis of γ-Bi_2MoO_6 by co-precipitation method and evaluation for photocatalytic degradation of rhodamine B, crystal violet and orange II dyes under visible light irradiation, Asian J. Chem. 30 (2018) 97–102.
[38] Y. Shimodaira, H. Kato, H. Kobayashi, A. Kudo, Photophysical properties and pbotocatalytic activities of bismuth molybdates under visible light irradiation, J. Phys. Chem. B 110 (2006) 17790–17797.
[39] M.T. Le, L.H. Bac, I. Van Driessche, S. Hoste, W.J.M. Van Well, The synergy effect between gamma and beta phase of bismuth molybdate catalysts: is there any

relation between conductivity and catalytic activity, Catal. Today 131 (2008) 566–571.
[40] Z.J. Zhang, X.Y. Chen, Sb_2MoO_6, Bi_2MoO_6, Sb_2WO_6, and Bi_2WO_6 flake-like crystals: generalized hydrothermal synthesis and the applications of Bi_2WO_6 and Bi_2MoO_6 as red phosphors doped with Eu^{3+} ions, Mater. Sci. Eng. B. 209 (2016) 10–16.
[41] C. Kongmark, V. Martis, A. Rubbens, C. Pirovano, A. Löfberg, G. Sankar, E. Bordes-Richard, R.-N. Vannier, W. Van Beek, Elucidating the genesis of Bi_2MoO_6 catalyst by combination of synchrotron radiation experiments and Raman scattering, Chem. Commun. (2009) 4850.
[42] H. Xie, D. Shen, X. Wang, G. Shen, Microwave hydrothermal synthesis and visible-light photocatalytic activity of γ-Bi_2MoO_6 nanoplates, Mater. Chem. Phys. 110 (2008) 332–336.
[43] T. Zhou, J. Hu, J. Li, Er^{3+} doped bismuth molybdate nanosheets with exposed {010} facets and enhanced photocatalytic performance, Appl. Catal. B Environ. 110 (2011) 221–230.
[44] C. Xu, D. Zou, L. Wang, H. Luo, T. Ying, γ-Bi2MoO6 nanoplates: surfactant-assisted hydrothermal synthesis and optical properties, Ceram. Int. 35 (2009) 2099–2102.
[45] J. Bai, Y. Li, J. Liu, L. Liu, 3D Bi_2MoO_6 hollow mesoporous nanostructures with high photodegradation for tetracycline, Microporous Mesoporous Mater. 240 (2017) 91–95.
[46] W. Huang, S. Ding, Y. Chen, W. Hao, X. Lai, J. Peng, J. Tu, Y. Cao, X. Li, 3D NiO hollow sphere/reduced graphene oxide composite for high-performance glucose biosensor, Sci. Rep. 7 (2017) 5220.
[47] S.N.A. Mohd Yazid, I. Md Isa, S. Abu Bakar, N. Hashim, S. Ab Ghani, A review of glucose biosensors based on graphene/metal oxide nanomaterials, Anal. Lett. 47 (2014) 1821–1834.
[48] R. Parvizi, S. Azad, K. Dashtian, M. Ghaedi, H. Heidari, Natural source-based graphene as sensitising agents for air quality monitoring, Sci. Rep. 9 (2019) 1–15.
[49] X.F. Shen, X.P. Yan, Facile shape-controlled synthesis of well-aligned nanowire architectures in binary aqueous solution, Angew. Chem. Int. Ed. 46 (2007) 7659–7663.
[50] C. Synthesis, L. Mos, G. Composites, E.E. Performances LI, Batteries, L -Cysteine-Assisted Synthesis of Layered MoS_2/Graphene Composites with Excellent Electrochemical Performances for Lithium Ion Batteries, 2011, pp. 4720–4728.
[51] M. Mazaheri, H. Aashuri, A. Simchi, Three-dimensional hybrid graphene/nickel electrodes on zinc oxide nanorod arrays as non-enzymatic glucose biosensors, Sensor. Actuator. B Chem. 251 (2017) 462–471.
[52] J.U. Lee, W. Lee, S.S. Yoon, J. Kim, J.H. Byun, Site-selective immobilization of gold nanoparticles on graphene sheets and its electrochemical properties, Appl. Surf. Sci. 315 (2014) 73–80.
[53] A. Khazraei, A. Tarlani, N. Naderi, J. Muzart, Z. Abdulhameed Kaabi, M. Eslami-Moghadam, Enhanced release and drug delivery of celecoxib into physiological environment by the different types of nanoscale vehicles, Appl. Surf. Sci. 422 (2017) 873–882.
[54] Z.Q. Li, X.T. Chen, Z.L. Xue, Bi_2MoO_6 microstructures: controllable synthesis, growth mechanism, and visible-light-driven photocatalytic activities, CrystEngComm 15 (2013) 498–508.
[55] J. Long, S. Wang, H. Chang, B. Zhao, B. Liu, Y. Zhou, W. Wei, X. Wang, L. Huang, W. Huang, Bi_2MoO_6 nanobelts for crystal facet-enhanced photocatalysis, Small 10 (2014) 2791–2795.
[56] Y. Li, Y. Wu, B.S. Ong, Facile synthesis of silver nanoparticles useful for fabrication of high-conductivity elements for printed electronics, J. Am. Chem. Soc. 127 (2005) 3266–3267.
[57] M.A. Ben Aissa, B. Tremblay, A. Andrieux-Ledier, E. Maisonhaute, N. Raouafi, A. Courty, Copper nanoparticles of well-controlled size and shape: a new advance in synthesis and self-organization, Nanoscale 7 (2015) 3189–3195.
[58] A. Phuruangrat, S. Putdum, P. Dumrongrojthanath, S. Thongtem, T. Thongtem, Hydrothermal Synthesis of Bi_2MoO_6 Visible-Light-Driven Photocatalyst, 2015, p. 2015.
[59] J. Zhao, Q. Lu, C. Wang, S. Liu, One-dimensional Bi_2MoO_6 nanotubes: controllable synthesis by electrospinning and enhanced simulated sunlight photocatalytic degradation performances, J. Nanoparticle Res. 17 (2015).
[60] B. Zhang, X. Ye, W. Hou, Y. Zhao, Y. Xie, Biomolecule-assisted synthesis and electrochemical hydrogen storage of Bi_2S_3 flowerlike patterns with well-aligned nanorods, J. Phys. Chem. B 110 (2006) 8978–8985.
[61] D. McNulty, D.N. Buckley, C. O'Dwyer, Optimizing the structure and yield of vanadium oxide nanotubes by periodic 2D layer scrolling, RSC Adv. 6 (2016) 40932–40944.
[62] S. Rastgar, S. Shahrokhian, Nickel hydroxide nanoparticles-reduced graphene oxide nanosheets film: layer-by-layer electrochemical preparation, characterization and rifampicin sensory application, Talanta 119 (2014) 156–163.
[63] L. Sim, C. Lee, A. West, High oxide ion conductivity in Bi_2MoO_6 oxidation catalyst, J. Mater. Chem. 12 (2002) 17–19.
[64] W. Mao, B. Cai, Z. Ye, J. Huang, A nanostructured p-NiO/n-$Bi_4Ti_3O_{12}$ heterojunction for direct GOx electrochemistry and high-sensitivity glucose sensing, Sensor. Actuator. B Chem. 261 (2018) 385–391.
[65] G. qing Liu, H. Zhong, X. rong Li, K. Yang, F. fei Jia, Z. peng Cheng, L. li Zhang, J. zhou Yin, L. ping Guo, H. yan Qian, Research on nonenzymatic electrochemical sensor using HO-$BiONO_3$ nanocomposites for glucose detection, Sensor. Actuator. B Chem. 242 (2017) 484–491.
[66] H. Liu, G. Xu, J. Wang, J. Lv, Z. Zheng, Y. Wu, Photoelectrochemical properties of TiO_2 Nanotube Arrays Modified with BiOCl nanosheets, Electrochim. Acta 130 (2014) 213–221.
[67] S. Wang, S. Zhang, M. Liu, H. Song, J. Gao, Y. Qian, MoS_2 as connector inspired high electrocatalytic performance of $NiCo_2O_4$ nanoplates towards glucose, Sensor. Actuator. B Chem. 254 (2018) 1101–1109.
[68] Z. Gao, Y. Lin, Y. He, D. Tang, Enzyme-free amperometric glucose sensor using a glassy carbon electrode modified with poly(vinyl butyral) incorporating a hybrid nanostructure composed of molybdenum disulfide and copper sulfide, Microchim. Acta. 184 (2017) 807–814.
[69] X. Li, X. Du, Molybdenum disulfide nanosheets supported Au-Pd bimetallic nanoparticles for non-enzymatic electrochemical sensing of hydrogen peroxide and glucose, Sensor. Actuator. B Chem. 239 (2017) 536–543.
[70] D. Geng, X. Bo, L. Guo, Ni-doped molybdenum disulfide nanoparticles anchored on reduced graphene oxide as novel electroactive material for a non-enzymatic glucose sensor, Sensor. Actuator. B Chem. 244 (2017) 131–141.
[71] L.F. Ang, L.Y. Por, M.F. Yam, Development of an amperometric-based glucose biosensor to measure the glucose content of fruit, PloS One 10 (2015) 1–17.
[72] F. Zhou, W. Jing, Y. Xu, Z. Chen, Z. Jiang, Z. Wei, Performance enhancement of ZnO nanorod-based enzymatic glucose sensor via reduced graphene oxide deposition and UV irradiation, Sensor. Actuator. B Chem. 284 (2019) 377–385.